Full length article

Predicting failure progressions of structural materials via deep learning based on void topology

Leslie Ching Ow Tiong [a,1], Gunjick Lee [b,1], Gyeong Hoon Yi [a,b], Seok Su Sohn [b,*], Donghun Kim [a,*]

[a] *Computational Science Research Center, Korea Institute of Science and Technology, Seoul 02792, Republic of Korea*
[b] *Department of Materials Science and Engineering, Korea University, Seoul 02841, Republic of Korea*

ARTICLE INFO

ABSTRACT

Despite considerable mechanics modeling-based efforts, accurate predictions of failure progressions of structural materials remain challenging in real-world environments primarily due to complex damage factors and defect evolutions. Here, we report a novel deep learning-based method for predicting failure properties based on defect state evolutions, which enables the full reflection of the damage accumulated in a material until the time of its examination. The method uniquely combines nondestructive X-ray computed tomography (X-CT), persistent homology (PH), and deep learning. It exploits the PH-encoded features from 3D X-CT images as its only input, and outputs failure-related properties. Using two fracture datasets based on low-alloy ferritic steel as a representative structural material, the method was demonstrated to reliably classify or predict the local strain (tensile dataset) and fracture progress (fatigue dataset). The excellent deep learning performances are attributed to both PH analysis and multimodal learning, where key topological features of internal voids, such as their size, density, and distributions, are precisely quantified. The proposed method enables accurate prediction of failure-related properties at the time of material examination based on void topology progressions, and can be extended to various nondestructive failure tests for practical use.

1. Introduction

Structural materials are designed to withstand the various damage factors that exist in application environments. Despite considerable research on material fatigue damage in recent decades, accurate predictions of the material lifetime remain challenging due to the complexity and high variability of real-world environments [1–8]. In fact, unexpected accidents caused by material failure have recently occurred, including aircraft disintegration in the air, building/bridge collapses, gas pipeline explosions, and container ships sinking [9–13]. These accidents have resulted in significant loss of life and property and, in severe cases, hundreds of casualties. These losses can be minimized by predicting when a material will fail and adopting preventative actions before material failure. Thus, methods for quantitatively predicting failure-related properties in environments where various factors, including load, heat, and corrosion, may comprehensively damage materials are crucial [14–18].

Models for predicting the failure behaviors and lifetimes of structural materials have been extensively studied for decades. Examples primarily include the mechanics-based finite element method (FEM) combined with the Gurson-Tvergaard-Needleman model, the Gunawardena model, and the continuum damage mechanics model [19–25]. The FEM has facilitated fatigue life predictions based on inputs such as the variation in yield locus under repeated loading cycles and the corresponding stress-life cycle curves (*S-N* curves). In addition, the geometry of the material can be considered, and the FEM has no constraints on the loading and boundary conditions applied to the materials [19,26–29]. However, this mechanics-based approach is limited in its ability to represent microstructural defects that develop differently depending on the exposed environmental factors. In this regard, a crystal plasticity FEM (CPFEM) has recently been explored to investigate the influences of microscopic scale features, including the evolution of microstructural defects such as voids and grains [28–32]. This method elucidates the stress–strain states near defects such as inclusions and pores, as well as

---

their effects on crack propagation and fatigue lifetime [33].

Nevertheless, it remains difficult to reflect the statistical information of defects, such as the evolution of their fraction, size, and distribution at each failure progression due to prohibitive computational costs, limiting the connections between microstructures and macro-properties at different length scales (*e.g.*, microstructural defect—strain state—fatigue lifetime). In this respect, data-driven machine learning (ML) approaches can overcome this scale gap since ML is capable of understanding correlations within datasets regardless of their length or time scale. Owing to these benefits, various ML techniques, such as random forests, support vector machines, and neural networks, have recently been used to predict the mechanical properties of metal systems, including their hardness [34,35], tensile properties [36,37], and crack propagation [38,39]. However, these ML models rely primarily on technical parameters such as experimental processing conditions as inputs, and no ML models have yet to be developed based on microstructural defect state that are obtained nondestructively, which is both a fundamental cause of failure and a critical requirement for predicting failure progressions in real-world application environments.

In this work, we propose a deep learning-based method to predict the failure properties of structural materials based on their defect states. In this study, the X-ray computed tomography (X-CT) is used to nondestructively monitor the evolution of the defect states, and persistent homology (PH) is used to quantify the void topology within complex 3D X-CT data. Our method takes PH-encoded results from X-CT images as its only input, and outputs the failure-related properties, such as the local strain and fracture progress. The effectiveness of the method was demonstrated using two fracture datasets, which were produced by tensile and fatigue testing of low-alloy ferritic steel as a representative structural material. The method reliably predicted the local strain (tensile dataset) and fracture progress (fatigue dataset), achieving mean absolute errors (MAEs) of only 0.09 and 0.14, respectively. These values are significantly lower than the MAEs of 0.55 and 0.57 obtained for cases without PH-based encoding. The remarkable performance enhancements are due to both PH process and multimodal learning, where key topological features of internal voids, such as their size, density, and distribution, were precisely quantified. The developed workflow could be easily extended to other nondestructive scanning methods, including phased array ultrasonic testing, for practical use.

2. Material and method

2.1. Design framework

Fig. 1 illustrates the overall scheme of our deep learning method, and Supplementary Fig. 1 shows the full test set-up images at each experimental and modeling stage. This method takes X-CT images of structural materials at the time of examination as its only input and outputs the failure-related properties. For model development and validation, in this study, we construct two types of fracture datasets: one produced by tensile mechanical testing and one produced by fatigue mechanical testing. The two datasets output different predictions: the tensile test outputs the local strain, and the fatigue test outputs the fracture progress. X-CT scanning can identify the positions and shapes of vacant regions, such as voids or cracks, in structural materials. Next, the X-CT images are processed by a combination of PH and deep learning. The 3D X-CT images are encoded into 2D persistence diagram (PD) via PH processing. This PH encoding step is an important innovation of this work since the patterns in 3D X-CT images are often too irregular and noisy to be directly used as the input of the following machine learning process. On the other hand, 2D PDs compressively capture and quantify key topological and geometrical features of defects in materials, such as their size, shape, density, and distribution. Thus, instead of the raw X-CT data, the transformed PDs are used as inputs to the ML process to predict failure-related properties, such as local strains or the fracture progress.

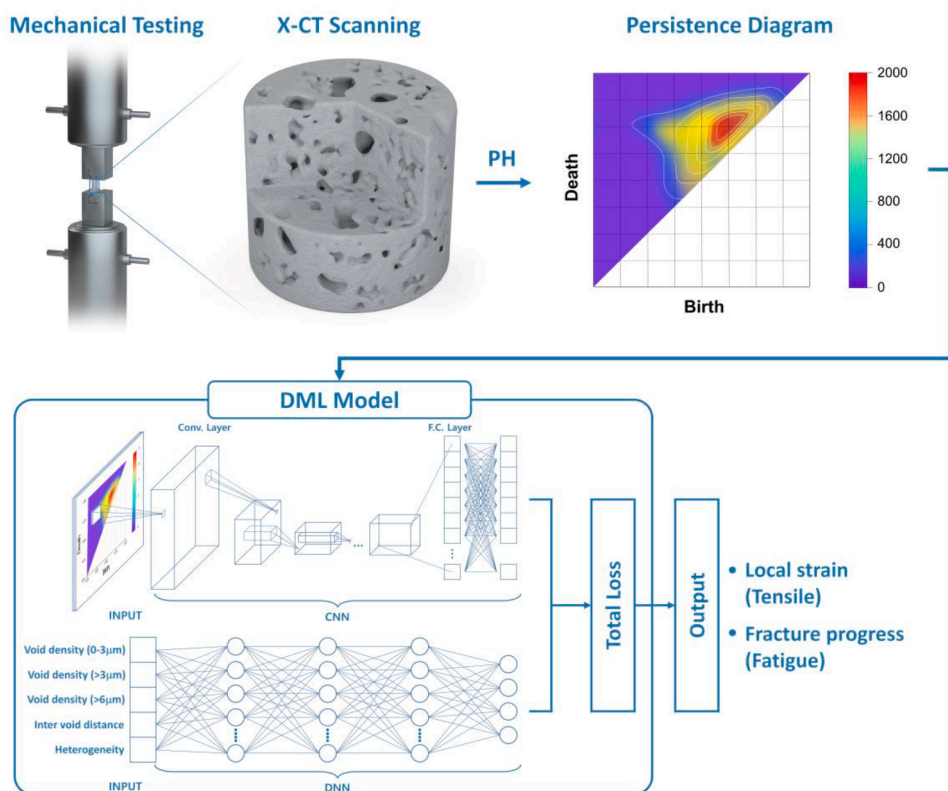In Fig. 1, among all ML models tested in this work, the deep

Fig. 1. Scheme of the proposed method. The method accepts X-CT images containing defect information as its sole input and outputs the failure-related properties at the time of material examination, such as the local strain for the tensile test and the fracture progress for the fatigue test.

multimodal learning (DML) model is representatively schematized due to its outstanding performance over benchmark models. Unlike the other models, which rely on a single input source, the DML model is multimodal and accepts two types of inputs: the PD images themselves and PD-extracted metrics. The PD-extracted metrics include the metrics extracted from PDs that quantify the void density, intervoid distance, and heterogeneity of void distributions. For the DML model to process the heterogeneous inputs of image data and value-type data,

convolutional neural networks (CNNs) and deep neural networks (DNNs) are used in parallel. We found that a DML model with two input sources considerably outperformed other benchmark models with a single input source. The PH and DML processing of the 3D X-CT data is our unique approach and key strategy for quantitatively predicting failure-related properties at the time of material examination.
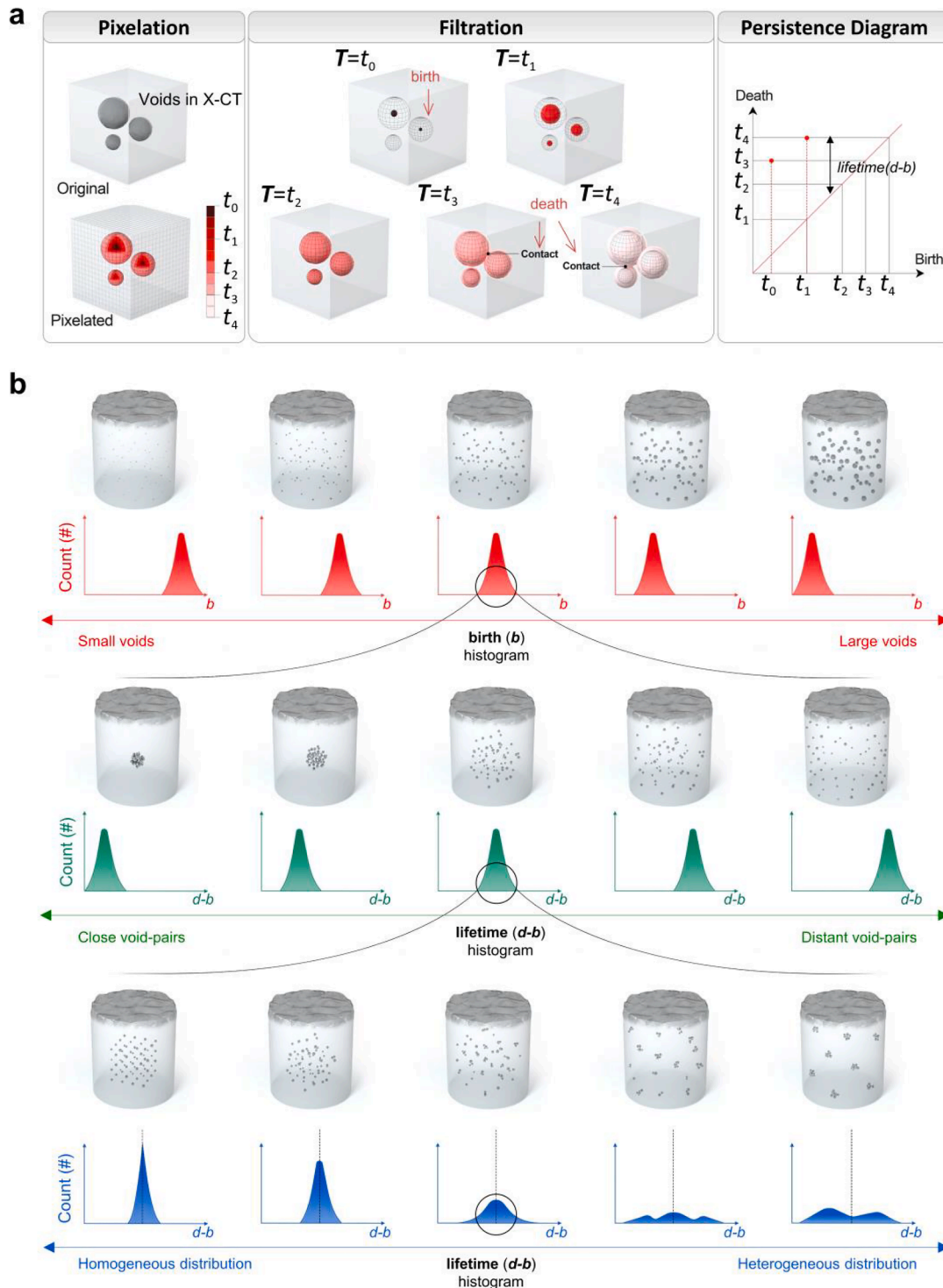

Fig. 2. PH process for measuring void topological features. (a) Scheme describing the PH process and the 0th PD computation. (b) Fifteen exemplary cases with different void topologies. The samples in the top row have different void sizes, the samples in the middle row have different intervoid distances, and the samples in the bottom row have different distributional heterogeneities. The corresponding birth (*b*) and lifetime (*d-b*) histograms are displayed.

2.2. Material fabrication

The low-alloy ferritic steel used in this work is composed as follows: (<0.05)C– (<1.7)Mn– (<0.3)Si– (<0.4)(Cr+Mo)– (<0.15)(Ti+Nb+V) (wt.%). The steel plate was homogenized at 1200–1250 °C for 1 h, hot-rolled to 800–850 °C, and cooled and coiled at 500–550 °C. The final thickness of the fabricated plate was 6.5 mm.

2.3. X-CT measurement and image processing

An X-ray microscope (ZEISS Xradia 520 Versa) was used. The output voltage, power, and step size of the X-CT scanning measurement were 160 kV, 10 W, and 3 μm, respectively. To obtain 3D binary format images (voids *versus* remaining background) from the X-CT data, we used an image processing approach, namely, window leveling, as illustrated in Supplementary Fig. 2. This approach aims to control the contrast within the possible range to remove the background and discern the void parts. As a result, the processed X-CT images are converted to 3D binary format images B as follows:

$$B(u, v) = \begin{cases} 255, & if \ I(u, v) > \alpha \\ 0, & otherwise \end{cases}$$

where $I(u, v)$ represents the pixel intensity, u and v are the pixel coordinates, and α is a threshold that is defined as 128 in this study.

2.4. PH process for quantifying void topology

Topological data analysis (TDA) is an emerging mathematical tool that uses algebraic topology principles to comprehensively measure shapes in datasets. TDA has shown promises in various application domains, including materials science, as it detects essential topological features embedded in a system by tracking the lifetime of *holes* in each dimension, such as connected components, loops, and voids [40–44]. TDA is often narrowly used to describe a particular subfield, namely, PH. In this work, PH is used to identify and quantify topological and geometric features in 3D X-CT images [45].

We compute the 0th PD via the pH process, and the intuitive idea underlying the PH process is illustrated in Fig. 2a. In a schematic example where the 3D X-CT scanning data contain multiple voids, the data can be mathematically regarded as 3D binary format data with void regions *versus* the remaining background region. The first step in the PH process is *pixelation,* where each pixel in the 3D space is assigned a number, such as t_0, t_1, t_2, t_3, t_4 and so forth (with pixels inside voids assigned values of $\leq t_2$ and pixels outside voids assigned values of $>t_2$) to be used in the subsequent PD computations. The rule for assigning these numbers is known as the Manhattan distance, and the number assigned at boundary surfaces (t_2 in Fig. 2a) is usually referenced to zero [41,46]. The next step is *filtration,* in which the union of pixels with assigned numbers less than a threshold value T is analyzed. When the threshold T is increased from t_0 to t_4, some islands appear (birth) and disappear (death), and the event times of these birth and death pairs are encoded in the 0th PD. When T equals to t_3 or t_4, the neighboring islands are observed to be in contact and combined into one body, and the smaller island is treated as a death. For the example shown in Fig. 2a, the (birth, death) pairs of (t_0, t_3) and (t_1, t_4) are finally encoded in the 0th PD.

Fig. 2b illustrates the information stored in the 0th PDs using 15 exemplary cases with different void topologies. Instead of PD images, we introduce birth (*b*) and lifetime (*d-b*) histograms, which can be obtained from simple reconstructions of the PD results, to more intuitively understand how different void topologies are reflected in the PD results. If the number of voids in a sample is assumed to be constant, the void topology can be varied by modifying three features: the void size, intervoid distance, and void distributional heterogeneity. The variations in each feature are schematized in three rows in Fig. 2b. For the samples in the top row, the void topology differs only in terms of the void size,

with the relative positions and distributions of the voids unchanged. Since larger voids appear earlier in the *filtration* process, peaks in the birth (*b*) histograms are shifted to the left (smaller birth values) for cases with larger voids. Next, we compare samples in the middle row of Fig. 2b, which exhibit different distributional features, namely, different intervoid distances. Since distant void pairs have longer void lifetimes in the *filtration* process, these differences should be reflected in the lifetime (*d-b*) histograms, and peaks in the histograms are shifted to the right (larger lifetime values) for distant void pairs. The last feature is the void distributional heterogeneity, which is schematized in the bottom row of Fig. 2b. The difference in heterogeneity is related to the degree of variation in the lifetime (*d-b*) histograms. Void lifetime values should be similar for homogeneous distributions, whereas these values vary substantially for heterogeneous cases. Overall, the PH processing of the 3D X-CT data can extract and quantify key topological features, including the void density, void size and some distributional features such as the intervoid distance and void heterogeneity. These PH capabilities are evaluated using two experimental fracture datasets obtained from different mechanical tests: one obtained from tensile tests and the other obtained from fatigue tests of metallic materials.

We used the PH processing API–HomCloud [47] to compute the 0th PD for the 3D binary format images. To compute the PD-extracted metrics, we first define D, the average intervoid distance, as the geometric mean of the lifetime (*d-b*) values, which can be calculated as follows:

$$D = \sqrt[M]{\prod_{i=1}^{M} d_i - b_i,}$$

where M is the total number of void pairs, and b_i and d_i refer to the birth and death times of the ith void pair. We also define V, the heterogeneity, as the degree of lifetime variations, which can be calculated as follows.

$$V = \sqrt[M]{\prod_{i=1}^{M} |(d_i - b_i) - D|}$$

2.5. Machine learning training protocol

For the experimental protocols, the dataset was randomly divided into a training set and a testing set with a ratio of 80:20 with no overlap. The samples in the training set were further divided for cross-validation purposes. The cross-validation protocol was designed as follows: (1) randomly shuffle the training set; (2) divide the training into five groups; (3) use one group as the validation set and the remaining groups as the training set; (4) repeat step (3) every 50 epochs and summarize the model evaluation scores. For the testing scheme, the testing set was used to evaluate the performance of our models. All network layer configurations are summarized in Supplementary Tables 1 and 2.

For the DML model, the networks were trained simultaneously. During training, we used an Adam optimizer [48] with a learning rate of 1.0×10^{-4}; the weight decay and momentum of the optimizer were defined as 1.0×10^{-8} and 0.9, respectively. We defined the total loss [49,50] (ℓ_{total}) function as the sum of the cross-entropies of the logit vectors, as well as their respective encoded labels, as follows:

$$l_{total} = l(FC_1) + l(FC_2),$$

$$l(FC_*) = -\sum_{k}^{K} \sum_{c}^{C} L_{kc} log[\delta(FC_*)_{kc}],$$

$$\delta(FC_*)_{kc} = \frac{exp^{(FC_*)_{kc}}}{\sum_{c}^{C} exp^{(FC_*)_{kc}}},$$

where * denotes the modal inputs (1 refers to PD images and 2 refers to PD-extracted metrics), *FC* is a fully connected layer, *L* denotes the class

labels, K is the number of training samples, C is the number of classes, and δ is the output layer, which is implemented with the softmax [51] function. For the prediction task, we used the following ℓ_{total} function:

$$l_{total} = l(\widehat{y}_1) + l(\widehat{y}_2)$$

$$l(\widehat{y}_*) = \sum_{i=1}^{n} \left(y_{i,*} - \widehat{y}_{i,*} \right)^2$$

where * denotes the modal inputs (1 refers to PD images and 2 refers to PD-extracted metrics), $\hat{y}$ is the predicted value, y denotes the actual value, and $\ell(\bullet)$ is defined as the mean square error loss function. The demonstration of the DML model is written in Python and TensorFlow toolkit, which is available at https://github.com/tiongleslie/material -failure-prediction.

3. Results

3.1. Dataset generation from tensile tests

We generated the fracture datasets used to develop the method shown in Fig. 1. Low-alloy ferritic steel, a representative structural material, is selected as the test material in this work [52,53]. The specimens used for the tensile test are plate-shaped, with a gauge length of a 6.4 mm and a thickness of 1.5 mm (inset of Fig. 3a). Tensile tests with a strain rate of 10^{-3} s^{-1} were performed on 15 ferritic steel specimens at room temperature. The total elongation when the sample broke was 40.7 $\pm$3.7% for these 15 samples, as shown in Fig. 3a and Supplementary Fig. 3. The digital image correlation (DIC) technique was used to measure the local strains of the samples, as shown in the local strain map in Fig. 3b. When a load is applied to a material, it deforms unequally, which means that some areas deform more and some areas deform less. The central part of the specimen near the fracture point was highly strained, exhibiting local strains of 100–130%. As the local strain varies substantially at different positions of the specimen, X-CT scanning was performed on multiple regions of the specimens (6–8 parts divided along the 6 mm length near the fractured surface).

Note that we recorded the void features from the fractured sample, which allows us to obtain a wide range of local strain values and diverse void features. Such a wide range can only be obtained for the specimen after the UTS point. Supplementary Fig. 4 shows the void features of the specimen with the engineering strain value of about 0.1 (corresponding to the UTS point). At this strain level, we observed that even the highest deformed region of the specimen exhibits little amounts of voids (only about 65 mm^{-3}). This indicates that, at the lower strain level (before the UTS point), void appearances were observed as only minimal. It was difficult to obtain samples of a wide range of local strain values, and of diverse void features, which adequately explains the reason why we recorded the void features from X-CT measurement of the fully extended and fractured specimen (much after the UTS point).

Although our specimen in this study was a miniature specimen with the gauge length of 6.4 mm, our approach of selecting the X-CT scanning
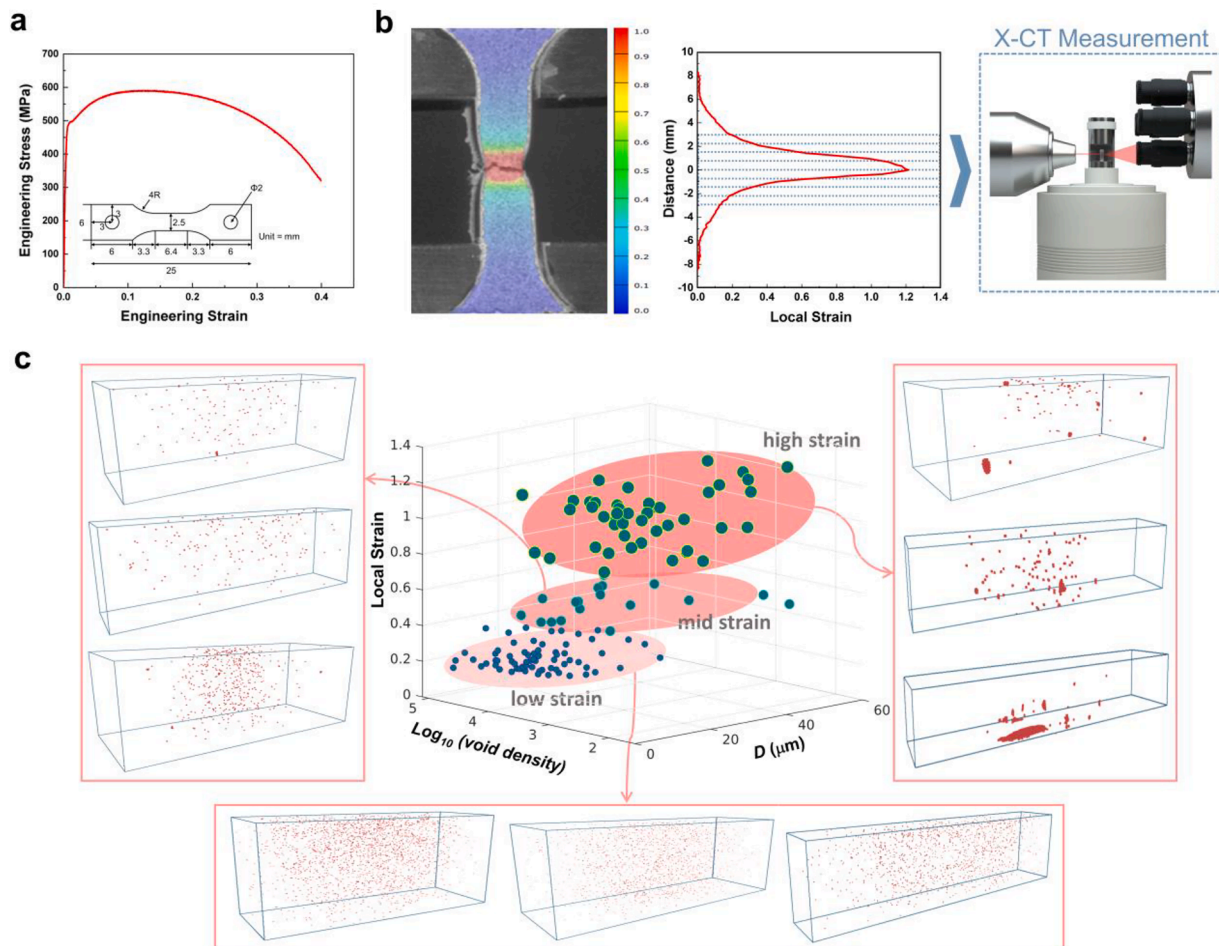

Fig. 3. A fracture dataset generated from tensile mechanical testing. (a) A representative engineering stress–strain curve of a test ferritic steel sample. The specimen dimensions are shown in the inset. (b) Local strain map and X-CT measurement process. An exemplary local strain map of the fractured sample obtained by the DIC technique is shown, with the color bar representing local strain values, as well as the corresponding strain profile. (c) The tensile dataset at a glance. The graph displays the local strain (z-axis) as a function of the void density (# mm^{-3}, log scale) and D (μm).

region is similarly applicable to the standard-shaped specimens. Supplementary Fig. 5 compares the DIC results of the miniature specimen with the gauge length of 6.4 mm (the original specimen used in this study) and the ASTM E8 specimen (a representative standard-shaped one). For the former, the X-CT scanning was performed along 6 mm near the fractured surface, and the local strain values range between 0.17 and 1.2. On the other hand, for the latter (ASTM E8) specimen, we found a very similar distributions of the local strain values, which range between 0.15 to 1.4 along over 6 mm region near the fracture surface. Indeed, both specimens have similar distributions in terms of the local strain values, which supports that our range selection for the X-CT measurements was reasonable.

A total of 135 data points were collected in the tensile dataset, and each data point consists of X-CT images and the corresponding local strain value of the X-CT-scanned part of the specimen. Fig. 3c shows an overview of the tensile dataset, displaying the local strain of each data point as a function of the void density (# mm^{-3}) and average intervoid distance (D). The void density is defined as the number of voids divided by the scan volume, and D is defined in the Methods section as the geometric mean of the lifetime (d-b) values in the PDs. The whole dataset can be roughly classified into regions with low, mid, and high local strains. As the strain increases from low to high, the void density tends to decrease, whereas D tends to increase. This tendency is visually confirmed in the internal void views revealed by X-CT scanning, where the voids decrease in number and increase in size, resulting in a larger value of D for high strain cases. The observed evolution of the void topology can be adequately explained by the void coalescence phenomenon, which is known to occur in ductile alloys under accumulated plastic deformations [54,55].

While Fig. 3c displays the overall dataset, Fig. 4 focuses on a specific specimen as an example for a more detailed PH analysis. A fractured ferritic steel sample is divided into four parts for the X-CT measurements
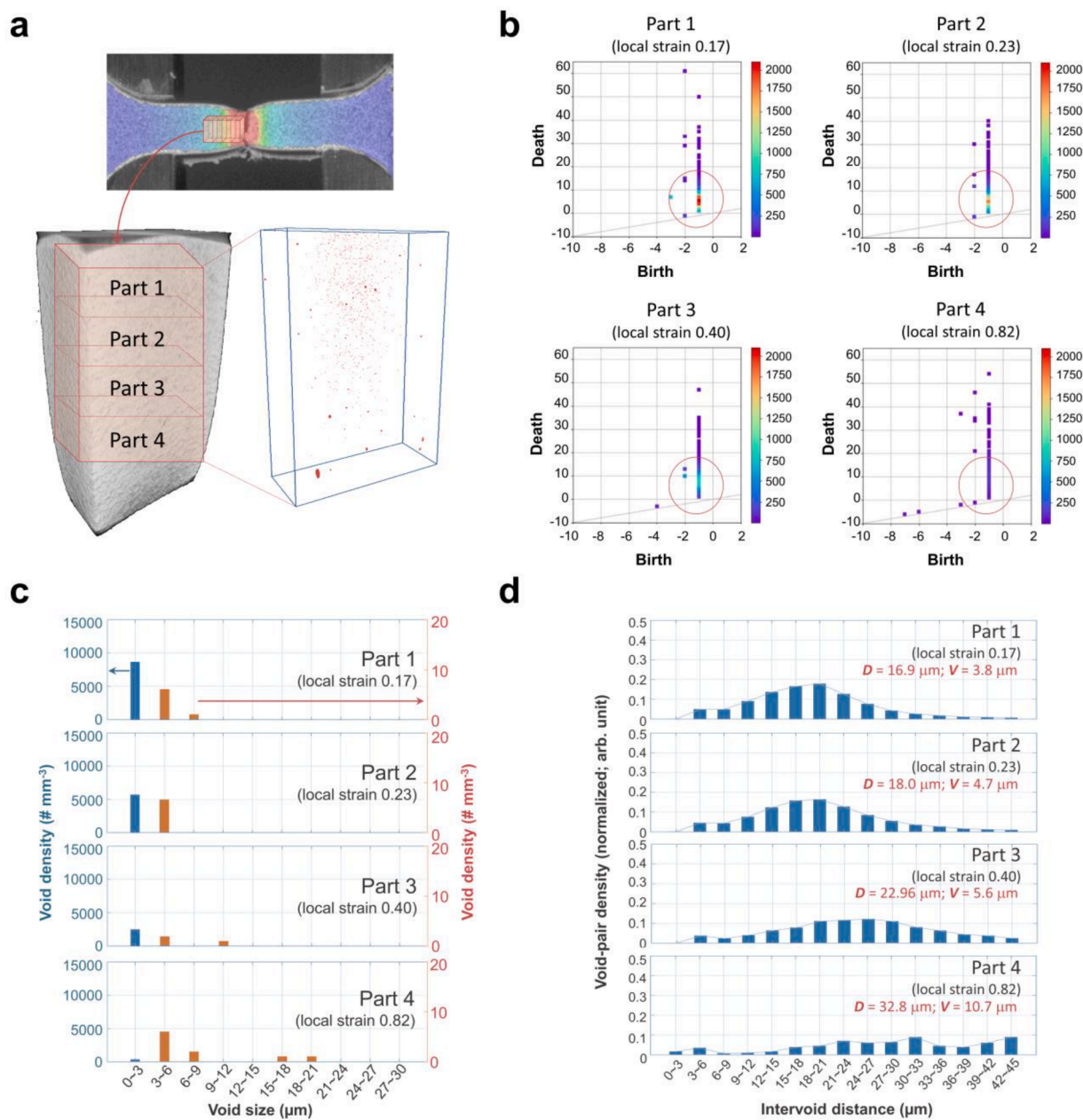

Fig. 4. PH analysis for a ferrite specimen fractured during tensile mechanical testing. (a) 3D structural view of fractured ferrite samples. The DIC result, X-CT overview, and internal void view are shown. (b) The 0th PDs of parts 1–4. (c) Birth (b) histograms. The left and right y-axes show the density of small voids ($\leq$3 μm) and larger voids ($>$3 μm), respectively. (d) Lifetime (d–b) histograms. The number of void pairs shown on the y-axis is normalized by the scanning volume.

(parts 1–4), with part 4 located nearest to the fractured surface. Each part is represented by different local strain values, namely, 0.17 (part 1), 0.23 (part 2), 0.40 (part 3), and 0.82 (part 4). In Fig. 4b, the 0th PDs for parts 1–4 are computed via the PH process introduced in Fig. 2a. These PDs are noticeably different from one another. In particular, as the local strain increases, the dot colors inside the red highlighted circles in Fig. 4b gradually change from red to purple, indicating that the density of the small voids (≤ 3 μm) substantially decreases.

In Fig. 4c and d, to more intuitively understand the quantitative difference in the void topology, birth (*b*) histograms and lifetime (*d-b*) histograms are built based on the PDs shown in Fig. 4b. Since the birth values are directly related to the void size (in this case, size $\approx -3 \times b$ μm because the unit length for each pixel in the pH process is 3 μm), the birth histogram summarizes the void size and density statistics. As the local strain increases (part 1 → part 4), the density of smaller voids (≤ 3 μm) rapidly decreases ($8638 \rightarrow 6047 \rightarrow 2634 \rightarrow 304$ mm^{-3}), whereas that of larger voids (3–21 μm) increases. This trend is consistent with the void coalescence phenomenon, in which small voids are combined into larger voids under heavy loads. Next, as the lifetime value represents the distance between neighboring voids (in this case, intervoid distance $\approx 3 \times (d–b)$ μm), the lifetime histogram presents the statistics of the void distributional features. *D*, which is defined as the geometric average intervoid distance, increases as the local strain increases ($D = 16.9 \rightarrow 18.0 \rightarrow 23.0 \rightarrow 32.8$ μm). Additionally, we introduce the void heterogeneity (*V*), which is defined as the degree of variation in the lifetime histograms. The equations for *D* and *V* are provided in the Methods

section. *V* also increases ($V = 3.8 \rightarrow 4.7 \rightarrow 5.6 \rightarrow 10.7$ μm) with increasing local strain. This PH analysis of the void topology of a ferrite specimen reveals that our method can quantify key void information such as size, density, and distributional features of intervoid distance and heterogeneity; thus, PD images and PD-extracted metrics (*D* and *V*) are suitable inputs for the subsequent ML studies.

3.2. Machine learning tensile dataset

We performed ML experiments with the tensile dataset to classify or predict local strains based on the pH results. Five ML models (Models I–V) are schematized in Fig. 5a. Although these models all output the local strain of the tested sample, the ML algorithms, architectures, and inputs all differ. The ML algorithms include multivariable linear regression [56] (MLR), DNN [57], and CNN [58]. In terms of input types, Model II differs from the other four models: Model II uses the raw X-CT images as inputs, whereas Models I, III, IV, and V use the PH results (PD images or PD-extracted metrics) as inputs. Here, the PD-extracted metrics include the following five metrics: void density (for void size ≤ 3 μm), void density (for void size of 3–6 μm), void density (for void size > 6 μm), *D*, and *V*. The void density is categorized into three classes based on the results of Fig. 4c, where the tendency of void density of small (≤ 3 μm) and larger (3–6 μm or > 6 μm) voids differed with local strain variations. For the MLR or DNN cases (Models I and III), PD-extracted metrics are used as inputs, while the CNN model (Model IV) uses the PD images as inputs since the CNN is a specialized algorithm
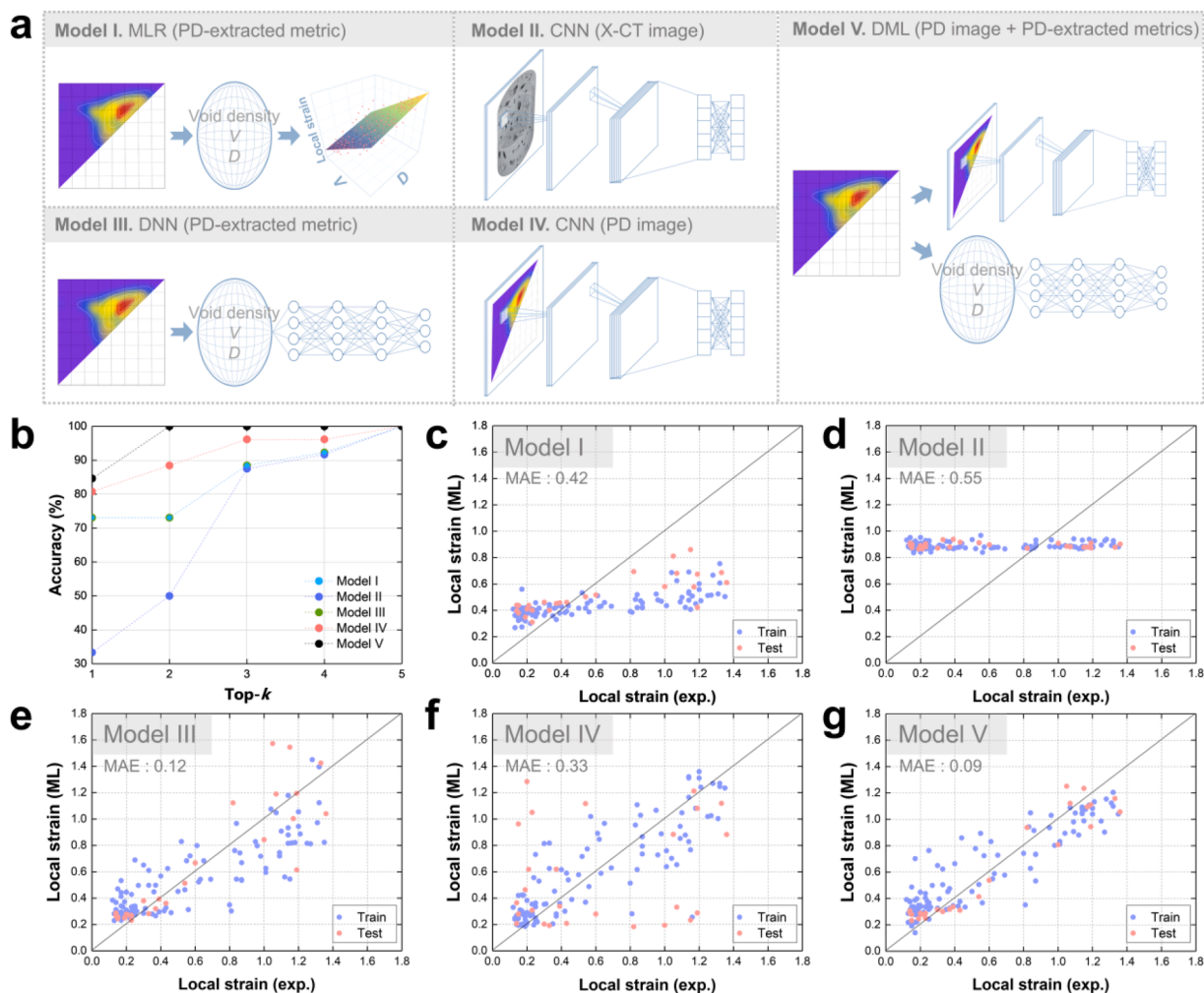

Fig. 5. ML results using the tensile dataset. (a) Schematics of the ML architecture and input types for Models I–V. (b) Top-*k* accuracies for the classifications of local strains. (c-g) Graphs comparing the local strains from experiments and ML predictions for Models I–V.

for processing images. For the DML model (Model V), Models III and IV are combined in parallel to utilize both PD images and PD-extracted metrics as inputs. The details of the network configurations are provided in Supplementary Tables 1 and 2.

First, ML classification tasks are performed using the tensile dataset. The local strain values range between 0.10–1.30 and can be categorized into five classes with 0.15 intervals: class #1: 0.10–0.25, class #2: 0.25–0.40, class #3: 0.40–0.55, class #4: 0.55–0.70, and class #5: $\geq$0.70. The accuracy results of the top-k classifications for Models I–V

are summarized in Fig. 5b. The top-k accuracy refers to the percentage of cases in which the correct class label appears among the top-k probabilities. Model V (DML model) showed an excellent performance, with a top-1 classification accuracy of 84.6% and 100% top-k ($k \geq 2$) accuracies. Model IV (CNN model based on PD images) also achieved a high top-1 accuracy of 80.8%. On the other hand, Models I and III, which are based on PD-extracted metrics, considerably underperformed, exhibiting accuracies of less than 75%. Model II, which is based on raw X-CT images, was inefficient, with a top-1 classification accuracy of only 31%.
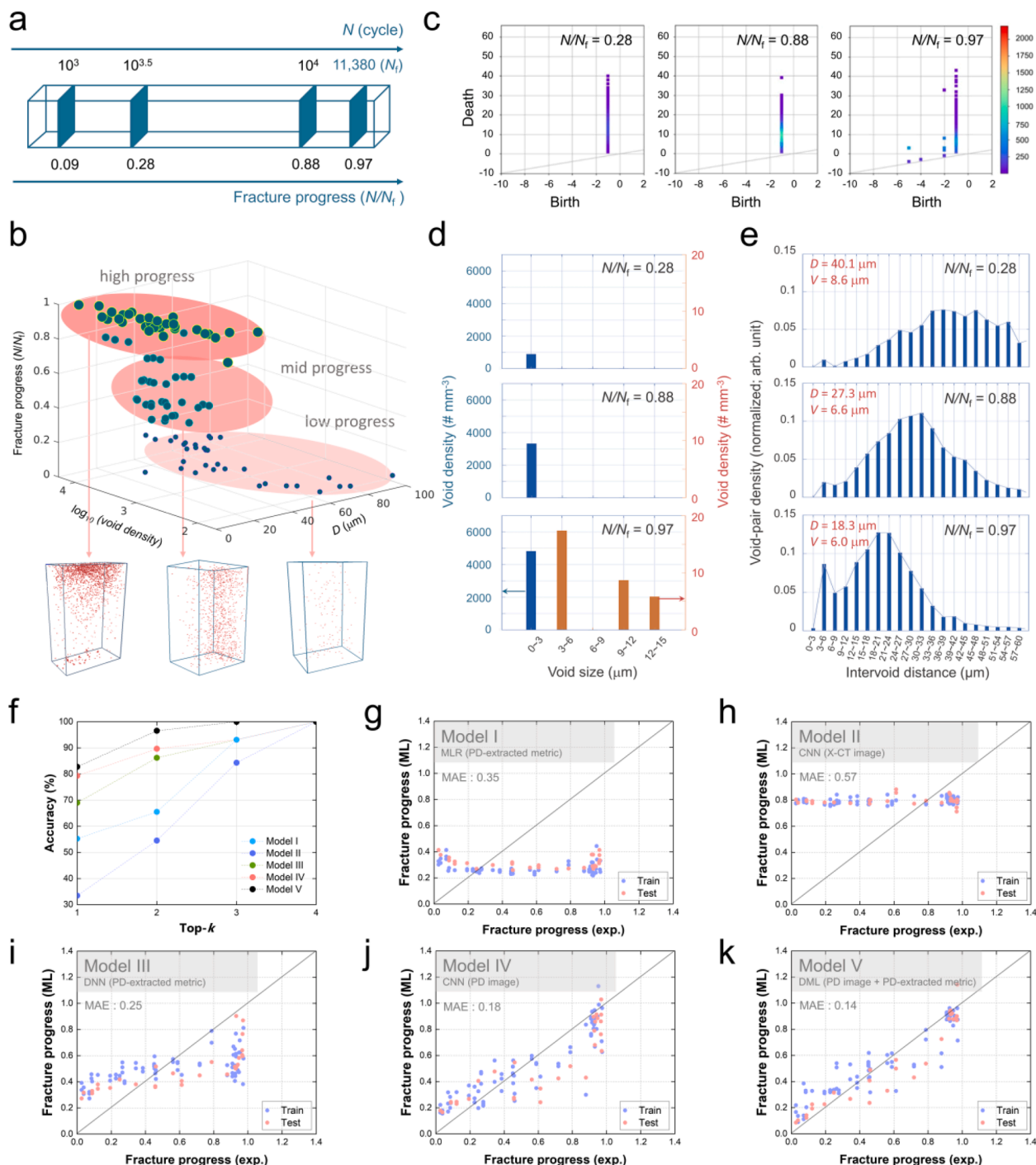

Fig. 6. Application of the developed method to the fatigue fracture dataset. (a) Scheme of data collection from fatigue tests. The X-CT data were obtained discretely at cycles of $10^{3.0}$, $10^{3.5}$, $10^{4.0}$, and $10^{4.5}$ and so forth until the specimen fails. (b) The fatigue dataset with X-CT images. The graph shows the fracture progress (N/N_f on the z-axis) as a function of the void density (# mm^{-3}, log scale) and D (μm). (c) The 0th PDs for representative samples with low, mid, and high progress. (d) Birth (b) histograms. (e) Lifetime (d–b) histograms. (f) Top-k accuracies for the classification of the fracture progress. (g–k) Graphs comparing fracture progress from experiments and ML predictions for Models I–V.

The very low performance of Model II, which does not use any PH-based inputs, demonstrates the effectiveness and necessity of PH-based encoding of noisy X-CT images.

Next, for the prediction tasks, all models are trained to predict, not classify, local strain values. The MAE is used to evaluate the prediction performance. Similar to the classification results, as shown in Fig. 5c–g, Model V (DML model) achieved the best MAE of 0.09. Model III achieved the second-lowest MAE of 0.12, and Models I and IV achieved MAEs of 0.42 and 0.33, respectively. Model II, which used raw X-CT images as inputs, performs the worst, exhibiting an MAE of 0.55, similar to the classification results, indicating that PH-based encoding is a necessary step to achieve high prediction performance.

Since Model V (our DML model) performs the best in both the classification and prediction tasks, it is worth investigating the reasons for these improvements. Model V includes two networks to exploit the different features of PD images and PD-extracted metrics. The two modal networks are based on a CNN and DNN; the former focuses on learning the features in the PD image, while the latter is trained on the PD-extracted metrics. The DML model simultaneously accepts and processes these different and complementary inputs and generates a joint feature representation to strengthen the feature activations of the network. This multimodal architecture is more effective at learning complex features than models that rely on a single input source.

3.3. Application to fatigue dataset

Figs. 3–5 show that the developed method is effective at classifying and predicting local strains using the tensile dataset. Our method was also applied to another fracture dataset, namely, the fatigue dataset, to predict fracture progressions. In real application environments, failure-induced accidents occur unexpectedly through fatigue mechanisms; thus, an expansion to a fatigue-driven fracture dataset is necessary for the method to be used as a practical and universal tool. The low-alloy ferritic steel was also used in the fatigue testing, and the specimens were plate-shaped, with a 3 mm gauge width and a 1.5 mm thickness. The detailed dimensions of the fatigue testing specimens are illustrated in Supplementary Fig 6. To induce void-driven fatigue fractures, the original ferrite specimens were intentionally prestrained with 10% tensile deformations before fatigue testing, causing small homogeneous voids to form within the specimens [59]. A fatigue uniaxial load was applied with a maximum stress of 700 MPa, an R-ratio of 0.1, and a frequency of 10 Hz. Fig. 6a illustrates the process of collecting the fatigue datasets. The fatigue tests were interrupted at cycles of 10^n ($n =$ 3.0, 3.5, 4.0, 4.5 and so forth) until the failure point for the X-CT measurements. The fracture progress of each specimen was then determined by dividing the interrupted cycle number (N) by the fatigue life cycle (N_f) of that specimen. For the exemplary case shown in Fig. 6a, the specimen was interrupted four times before it failed, at progresses of 9%, 28%, 88%, and 97%, and the defect topology evolutions in the gauge region of the specimens were obtained by X-CT scanning.

The fatigue dataset includes a total of 100 data points, and each data point is composed of X-CT images and the corresponding fracture progress. Fig. 6b illustrates the whole fatigue dataset in terms of the fracture progress (N/N_f), void density, and D. The data distribution can be classified into three categories, with low, mid, and high fracture progress. As the fracture progress increases from low to high, the void density tends to increase, resulting in a decrease in D. This tendency can be visually confirmed with the internal void views shown in Fig. 6b, and this tendency is a discriminative feature of ML studies, likely leading to a high prediction accuracy. Fig. 6c–e illustrate the 0th PD images and corresponding birth and lifetime histograms for representative samples with low, mid, and high fracture progress. These PD images differ mainly in the birth value range of -6 to -2, which indicates the appearance of larger voids (3–15 μm) in samples with higher progress. Quantitatively, in the birth histograms (Fig. 6d), as the progress increases, the density of small voids (≤3 μm) increases (877 → 3311 →

4826 mm^{-3}), while larger voids (3–15 μm) with densities of more than a few tens mm^{-3} typically form when the progress exceeds 90%. In terms of the distributional features stored in lifetime histograms (Fig. 6e), as the progress increases, D and V both decrease, with values of 40.1 → 27.3 → 18.3 μm and 8.6 → 6.6 → 6.0 μm, respectively. These results are consistent because an increase in the void number should cause the voids to be distributed in a closer and more homogeneous manner. These various PD features, including D and V, can discriminate samples with different fracture progresses and can thus be used as inputs in ML studies.

This trend in void features was observed quite universal for different batches of the same material from the same manufacturer. Supplementary Fig. 7 compares the void features including void size, density, and distribution information of several samples for very similar fracture progresses from two different batches (namely, batches A and B): 25% of the batch A vs. 28% of the batch B; 79% of the batch A vs. 88% of the batch B; and 97% of the batch A vs. 97% of the batch B. Supplementary Fig. 7 shows that void features were found very similar for three comparison cases from the batches A and B, which supports the very high similarity of void features. Thus, our method should work well even for the different batches of the same material from the same manufacturer.

ML experiments were carried out on the fatigue datasets to classify or predict the fracture progress. Models I–V, which are shown in Fig. 5, were also tested using the fatigue dataset. First, ML classification tasks were performed. The progress values can be categorized into the following four classes: class #1: ≤0.2, class #2: 0.2–0.5, class #3: 0.5–0.9, and class #4: 0.9–1.0. Note that the intervals between the four classes are not identical; instead, the intervals were adjusted to ensure that the amount of data in each category is similar. A uniform data distribution over all classes is necessary for unbiased ML predictions, particularly when the amount of data is small. The top-k classification accuracy results for Models I–V are summarized in Fig. 6f. Similar to the tensile case, Model V (DML model) performs the best, with top-1 and top-2 classification accuracies of 82.8% and 95.7%, respectively. Model IV (CNN model based on PD images) achieved the second-best performance, with for top-1 and top-2 accuracies of 79.3% and 92.4%, respectively. Models I and III, which are based on only PD-extracted metrics (no PD images), underperform, achieving top-1 classification accuracies of less than 70%. Model II, which utilizes raw X-CT images as its sole input source (no PH-based inputs), exhibits the worst top-1 accuracy of only 33%, indicating that ML training based on only raw X-CT data is not successful. Comparisons between Model II and the other models show that the PH process is an effective approach in machine learning for handling complex and noisy X-CT image data.

Next, for the prediction tasks, Models I–V are used to predict the fracture progress. Figs. 6g-6k show that, similar to the classification results, Model V (DML model) achieved the best MAE of 0.14, and Model IV achieved the second-best MAE of 0.18. Models I and III, which use PD-extracted metrics as inputs, showed worse MAEs of 0.35 and 0.25, respectively, indicating that PD-extracted metrics alone cannot sufficiently capture the essential void-related information required for ML training. Unsurprisingly, Model II, which does not use any PH-based inputs, exhibited the poorest MAE of 0.57, again supporting the difficulty of training with raw X-CT images. The performance enhancement of our DML model (Model V) over other benchmark models appears to be universal in both the tensile and fatigue datasets. Unlike most other ML models, which rely on single input sources, our DML model benefits from exploiting discriminatory features from two input sources, namely, PD images and PD-extracted metrics.

3.4. OSA analysis

Thus far, we confirmed that the combined PH and DL models provides the high prediction performances for failure progressions, and embodies the associated failure characteristics. Yet, it was not sufficiently understood which factors regarding the void topology play a

prior role for the reliable property predictions. In this regard, in Fig. 7, an occlusion sensitivity analysis (OSA) was performed for Models III and IV and for the tensile and fatigue datasets. OSA is used to quantify the importance of each input feature and can thereby identify key components learned by the models. Here, an occlusion process refers to partially hiding a specific feature of the input data, and the change in classification accuracy due to the occlusion is evaluated. This analysis reveals the sensitivity of output predictions to occluded input data.

The OSA results for Model IV (CNN based on PD images) and Model III (DNN based on PD-extracted metrics) are illustrated in Fig. 7a and b, respectively. For Model IV, the occlusion hides a specific location in the PD images, and the accuracy change due to each occlusion part was computed. Regions corresponding to the cluster of small voids (marked in black) were identified as highly sensitive spots, with occlusions causing an accuracy degradation of 15–35% for both the tensile and fatigue datasets. These results are consistent with previous observations that the void density of small voids (≤ 3 μm) is substantially affected by local strains (tensile) and fracture progress (fatigue), indicating that the development of small voids is a key learning feature. The OSA result for Model III in Fig. 7b reveals additional information. Unlike the CNN case, the occlusion in the DNN model involves changing a specific input data feature to a value of zero, and the effects of these occlusions on the output predictions were quantified. This test revealed that the density of small voids (≤ 3 um) and D are both critical learning features. The priority of these two features (void density for voids ≤ 3 μm and D) is reversed depending on the dataset used: the void density (≤ 3 um) is more important for the tensile dataset, while D is more important for the fatigue dataset.

4. Discussion

We describe the advantages and limitation of our method, compared to the existing methods which are mainly based on FEM or CPFEM approaches. These previous models were limited in reflecting the statistical information of real defects, such as the evolution of their fraction, size, and distributions at each failure progression, mainly due to prohibitive computational cost. On the other hand, our method is a data-driven approach (deep learning model) and thus is free from the time scale, as long as the dataset is prepared in a sufficient amount. Thus, our deep

learning-based method can easily predict failure properties over a wide range of time scales (for example, predictions from 0 to 100% fracture progress). Another benefit of our method is that it is fed with the X-CT image as its only input at the time of the material examination (real-time measurement). This enables the full reflection of the damage accumulated in a material until the time of its examination. Such real-time reflection of external factors is difficult for the FEM-based approach where the loading and environmental factors are typically given as initial inputs.

On the other hand, the limitation of our method is that the performance strongly depends on the dataset preparation. The property predictions cannot be accurate when the actual loading situation was not trained. In reality, the material is subject to various environmental loading conditions. In this work, our datasets were designed in fully controlled environments, with uniaxial tensile and fatigue tests conducted at room temperature. Thus, the developed tool may perform poorly in uncontrolled situations due to large differences with the training data. To overcome this limitation, datasets need to be constructed in more diverse experimental environments, in which the strain rates, fatigue modes, stress amplitudes, R-ratios, and temperatures can be crucial parameters.

In principle, if we want to apply our method to different types of materials, a completely new dataset based on the specific material need to be constructed for new ML training and tests. Nonetheless, to understand if our method would be useful for other ferritic steel materials possessing similar compositions and mechanical properties, we performed additional ML prediction studies using a different type of low-alloyed ferritic steel. Note that this new tested specimen has very similar elemental compositions (also follow in range (<0.05)C–(<1.7) Mn– (<0.3)Si–(<0.4)(Cr+Mo)–(<0.15)(Ti+Nb+V) wt.%), but different manufacturing processes (;higher extraction temperature, start rolling temperature, finish delivery temperature, reduction ratio; and lower coiling temperature) from the previously used one, and 11 samples which were not parts of our training set were used for ML tests. Our DML model achieved 72.7% for the classification task, and the MAE of the prediction task was found as 0.16. Overall, the accuracy of our DML model slightly dropped, however, the model still maintains its high performance compared to the reference models such as CNN and DNN. The high prediction and classification accuracy observed for the new
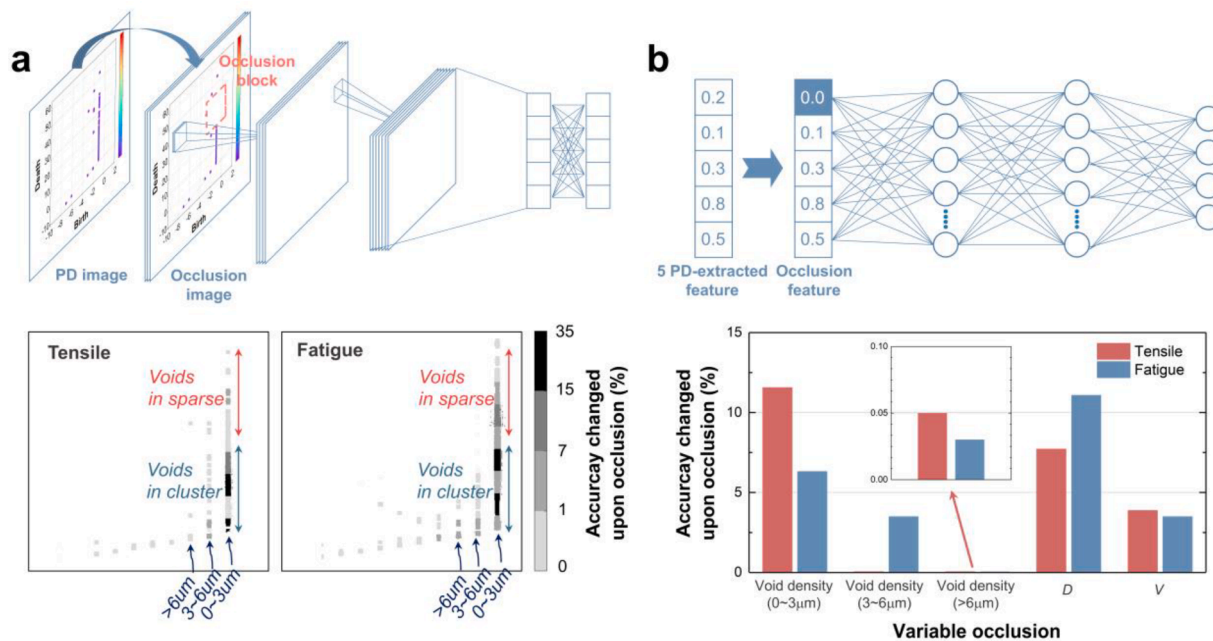

Fig. 7. OSA results. (a) Scheme illustrating the OSA process for Model IV (CNN based on PD images) and the corresponding accuracy changes with occlusions. (b) Scheme describing the OSA process for Model III (DNN based on PD-extracted metrics) and the corresponding accuracy changes with occlusions.

testing materials supports that our model can be well expanded to other ferritic steel materials with similar compositions, and indicates that the internal voids dictate the fracture properties for these materials.

We would like to clarify the capability of our developed method, in terms of what can be chosen as output properties. Our method is fed with the input of X-CT images of a deformed material, and outputs some mechanical properties at the specific and corresponding deformation level. Thus, these output properties should be the properties that are affected by the deformation level, which for example includes the local strain (from tensile tests) and fracture progress (from fatigue tests). On the other hand, our method is not suitable for predicting the engineering properties that are intrinsic to a given material, such as elastic modulus, yield stress/strain, and ultimate stress/strain. These mechanical properties are intrinsic properties for a given material, rather than properties being varied by the deformation level.

In addition to X-rays, our method can be applied to other types of nondestructive scanning tests, such as ultrasonic imaging measurements. Although we selected X-ray scans to obtain high-resolution characterizations of defects, X-ray scanning often investigates localized areas due to limited permeability issues in highly dense metal systems such as steels. On the other hand, ultrasonic testing offers the benefits of scanning wider and deeper areas and is thus considered a more suitable choice in industrial situations, despite its comparatively lower resolution. In fact, ultrasonic-based scanning, such as phased array ultrasonic testing (PAUT), is the most commonly used nondestructive scanning method in industry. Thus, our method should be expanded to fracture datasets obtained by PAUT for practical use.

5. Conclusions

In summary, we report a novel method based on a combination of X-CT, PH, and deep learning, which enables the reliable predictions of failure-related properties at the time of material's nondestructive examination. Since the method exploits the microstructural defect state obtained by the X-CT scanning as its input, it fully reflects the damaging factors accumulated in the material by the time of examination. Using both tensile and fatigue fracture datasets of low-alloy ferritic steel, the method achieves small MAEs of 0.09 and 0.14 in predicting the local strain and the fracture progress, respectively. These high accuracies are due to both PH-based encoding and multimodal learning, where noisy 3D X-CT images were transformed into 2D PDs that preserve key topological features such as the internal void size, density, and distribution. The combined PH and DML processing of 3D X-CT data is our unique computational approach enabling the failure predictions based on void topology progressions, and can be universally used for various mechanical datasets where void topology plays vital roles.

Declaration of Competing Interest

The authors declare that they have no known competing financial interests or personal relationships that could have appeared to influence the work reported in this paper.

Acknowledgments

Supplementary materials

Supplementary material associated with this article can be found, in the online version, at doi:10.1016/j.actamat.2023.118862.

References

[1] P. Temarel, W. Bai, A. Bruns, Q. Derbanne, D. Dessi, S. Dhavalikar, N. Fonseca, T. Fukasawa, X. Gu, A. Nestegård, A. Papanikolaou, J. Parunov, K.H. Song, S. Wang, Prediction of wave-induced loads on ships: progress and challenges, Ocean Eng. 119 (2016) 274–308.

[2] Y. Liu, S. Mahadevan, Multiaxial high-cycle fatigue criterion and life prediction for metals, Int. J. Fatigue 27 (2005) 790–800.

[3] F. Shen, B. Zhao, L. Li, C.K. Chua, K. Zhou, Fatigue damage evolution and lifetime prediction of welded joints with the consideration of residual stresses and porosity, Int. J. Fatigue 103 (2017) 272–279.

[4] F. Biondini, D.M. Frangopol, Probabilistic limit analysis and lifetime prediction of concrete structures, Struct. Infrastruct. E 4 (2008) 399–412.

[5] E.J. Tuegel, A.R. Ingraffea, T.G. Eason, S.M. Spottswood, Reengineering aircraft structural life prediction using a digital twin, Int. J. Aerosp. Eng. 2011 (2011) 154798.

[6] S. Amiable, S. Chapuliot, A. Constantinescu, A. Fissolo, A comparison of lifetime prediction methods for a thermal fatigue experiment, Int. J. Fatigue 28 (2006) 692–706.

[7] B. Fournier, M. Sauzay, C. Caës, M. Noblecourt, M. Mottot, A. Bougault, V. Rabeau, J. Man, O. Gillia, P. Lemoine, A. Pineau, Creep-fatigue-oxidation interactions in a 9Cr-1Mo martensitic steel. Part III: lifetime prediction, Int. J. Fatigue 30 (2008) 1797–1812.

[8] A. Yadollahi, M.J. Mahtabi, A. Khalili, H.R. Doude, J.C. Newman, Fatigue life prediction of additively manufactured material: effects of surface roughness, defect size, and shape, Fatigue Fract. Eng. Mater. Struct. 41 (2018) 1602–1614.

[9] G. Storhaug, The measured contribution of whipping and springing on the fatigue and extreme loading of container vessels, Int. J. Nav. Archit. 6 (2014) 1096–1110.

[10] Y. Zhu, X. ming Qian, Z. yi Liu, P. Huang, M. qi Yuan, Analysis and assessment of the Qingdao crude oil vapor explosion accident: lessons learnt, J. Loss Prev. Process Ind. 33 (2015) 289–303.

[11] W.C. Li, D. Harris, C.S. Yu, Routes to failure: analysis of 41 civil aviation accidents from the Republic of China using the human factors analysis and classification system, Accid. Anal. Prev. 40 (2008) 426–434.

[12] A.O. Windapo, J.O. Rotimi, Contemporary issues in building collapse and its implications for sustainable development, Buildings 2 (2012) 283–299.

[13] L. Deng, W. Wang, Y. Yu, State-of-the-art review on the causes and mechanisms of bridge collapse, J. Perform. Constr. Facil. 30 (2016), 04015005.

[14] C.G. Soares, Y. Garbatov, A. Zayed, G. Wang, Influence of environmental factors on corrosion of ship structures in marine atmosphere, Corros. Sci. 51 (2009) 2014–2026.

[15] G. Sposito, C. Ward, P. Cawley, P.B. Nagy, C. Scruby, A review of non-destructive techniques for the detection of creep damage in power plant steels, NDT E Int. 43 (2010) 555–567.

[16] C. Kong, J. Bang, Y. Sugiyama, Structural investigation of composite wind turbine blade considering various load cases and fatigue life, Energy 30 (2005) 2101–2114.

[17] Y. Bai, Marine Structure Design, Elsevier Science, Oxford, 2003.

[18] A. Iseda, H. Okada, H. Semba, M. Igarashi, Long term creep properties and microstructure of SUPER304H, TP347HFG and HR3C for A-USC boilers, Energy Mater. 2 (2007) 199–206.

[19] S. Abdullah, N.A. Al-Asady, A.K. Ariffin, M.M. Rahman, A review on finite element analysis approaches in durability assessment of automotive components, J. Appl. Sci. 8 (2008) 2192–2201.

[20] E. Santecchia, A.M.S. Hamouda, F. Musharavati, E. Zalnezhad, M. Cabibbo, M. el Mehtedi, S. Spigarelli, A review on fatigue life prediction methods for metals, Adv. Mater. Sci. Eng. 2016 (2016) 1–26.

[21] F. Rahimidehgolan, G. Majzoobi, F. Alinejad, J.Fathi Sola, Determination of the constants of GTN damage model using experiment, polynomial regression and kriging methods, Appl. Sci. 7 (2017) 1179.

[22] G.R. Johnson, W.H. Cook, Fracture characteristics of three metals subjected to various strains, strain rates, temperatures and pressures, Eng. Fract. Mech. 21 (1985) 31–48.

[23] A. Weck, J. Segurado, J. LLorca, D. Wilkinson, H. Böhm, Numerical simulations of void linkage in model materials using a nonlocal ductile damage approximation, Int. J. Fract. 148 (2007) 205–219.

[24] J.C. Boyer, E. Vidal-Sallé, C. Staub, A shear stress dependent ductile damage model, J. Mater. Process. Tech. 121 (2002) 87–93.

[25] H.W. Lee, C. Basaran, A review of damage, void evolution, and fatigue life prediction models, Metals 11 (2021) 609.

[26] G.C. Silva, V.C. Beber, D.B. Pitz, Machine learning and finite element analysis: an integrated approach for fatigue lifetime prediction of adhesively bonded joints, Fatigue Fract. Eng. Mater. Struct. 44 (2021) 3334–3348.

[27] M. Kikuchi, Y. Wada, Y. Shintaku, K. Suga, Y. Li, Fatigue crack growth simulation in heterogeneous material using s-version FEM, Int. J. Fatigue 58 (2014) 47–55.

[28] S.K. Ås, B. Skallerud, B. Tveiten, B. Holme, Fatigue life prediction of machined components using finite element analysis of surface topography, Int. J. Fatigue 27 (2005) 1590–1596.

[29] Barna Szabó, Ivo Babuska, Finite Element Analysis, Wiley-Interscience, 1991.

[30] U. Asim, M.A. Siddiq, M. Demiral, Void growth in high strength aluminium alloy single crystals: a CPFEM based study, Model. Simul. Mater. Sci. Eng. 25 (2017), 035010.

[31] U. bin Asim, M.A. Siddiq, M.E. Kartal, A CPFEM based study to understand the void growth in high strength dual-phase titanium alloy (Ti-10V-2Fe-3Al), Int. J. Plast. 122 (2019) 188–211.

[32] F. Roters, P. Eisenlohr, L. Hantcherli, D.D. Tjahjanto, T.R. Bieler, D. Raabe, Overview of constitutive laws, kinematics, homogenization and multiscale

methods in crystal plasticity finite-element modeling: theory, experiments, applications, Acta Mater. 58 (2010) 1152–1211.

[33] W. Zhang, Y. Hu, X. Ma, G. Qian, J. Zhang, Z. Yang, F. Berto, Very-high-cycle fatigue behavior of AlSi10Mg manufactured by selected laser melting: crystal plasticity modeling, Int. J. Fatigue 145 (2021), 106109.

[34] L. Qiao, Z. Lai, Y. Liu, A. Bao, J. Zhu, Modelling and prediction of hardness in multi-component alloys: a combined machine learning, first principles and experimental study, J. Alloy. Compd. 853 (2021), 156959.

[35] Y.J. Chang, C.Y. Jui, W.J. Lee, A.C. Yeh, Prediction of the composition and hardness of high-entropy alloys by machine learning, JOM 71 (2019) 3433–3442.

[36] W. ben Chaabene, M.N. Majdi Flah, Machine learning prediction of mechanical properties of concrete: critical review, Constr. Build. Mater. 260 (2020), 119889.

[37] X. Jiang, B. Jia, G. Zhang, C. Zhang, X. Wang, R. Zhang, H. Yin, X. Qu, Y. Song, L. Su, Z. Mi, L. Hu, H. Ma, A strategy combining machine learning and multiscale calculation to predict tensile strength for pearlitic steel wires with industrial data, Scr. Mater. 186 (2020) 272–277.

[38] S.N.S. Mortazavi, A. Ince, An artificial neural network modeling approach for short and long fatigue crack propagation, Comput. Mater. Sci. 185 (2020), 109962.

[39] A. Rovinelli, M.D. Sangid, H. Proudhon, W. Ludwig, Using machine learning and a data-driven approach to identify the small fatigue crack driving force in polycrystalline materials, Npj Comput. Mater. 4 (2018) 4–35.

[40] A. Zomorodian, G. Carlsson, Computing persistent homology, Discrete Comput. Geom. 33 (2005) 249–274.

[41] M. Kimura, I. Obayashi, Y. Takeichi, R. Murao, Y. Hiraoka, Non-empirical identification of trigger sites in heterogeneous processes using persistent homology, Sci. Rep. 8 (2018) 1–9.

[42] P. Bubenik, J.A. Scott, Categorification of persistent homology, Discrete Comput. Geom. 51 (2014) 600–627.

[43] A. Suzuki, M. Miyazawa, J.M. Minto, T. Tsuji, I. Obayashi, Y. Hiraoka, T. Ito, Flow estimation solely from image data through persistent homology analysis, Sci. Rep. 11 (2021) 1–13.

[44] M. Saadatfar, H. Takeuchi, V. Robins, N. Francois, Y. Hiraoka, Pore configuration landscape of granular crystallization, Nat. Commun. 8 (2017) 15082.

[45] M.A. Kader, A.D. Brown, P.J. Hazell, V. Robins, J.P. Escobedo, M. Saadatfar, Geometrical and topological evolution of a closed-cell aluminium foam subject to drop-weight impact: an X-ray tomography study, Int. J. Impact Eng. 139 (2020), 103510.

[46] S. Craw, C. Sammut, G.I. Webb, Manhattan distance. Encyclopedia of Machine Learning, Springer US, Boston, MA, 2010, p. 639.

[47] I. Obayashi, HomCloud (2021). https://homcloud.dev/index.en.html (accessed April 12, 2020).

[48] D.P. Kingma, J. Ba, Adam: a method for stochastic optimization, in: Proceedings of the International Conference on Learning Representations, San Diego, CA, 2015, pp. 1–13.

[49] A. Kendall, Y. Gal, R. Cipolla, Multi-task learning using uncertainty to weigh losses for scene geometry and semantics, in: Proceedings of the IEEE Conference on Computer Vision and Pattern Recognition (CVPR), Salt Lake City, UT, USA, 2018, pp. 7482–7491.

[50] L.C.O. Tiong, J. Kim, S.S. Han, D. Kim, Identification of crystal symmetry from noisy diffraction patterns by a shape analysis and deep learning, Npj Comput. Mater. 6 (2020) 1–11.

[51] S. Bruch, X. Wang, M. Bendersky, M. Najork, An analysis of the softmax cross entropy loss for learning-to-rank with binary relevance, in: Proceedings of the ACM SIGIR International Conference on Theory of Information Retrieval, Santa Clara, CA, USA, 2019, pp. 75–78.

[52] T.W. Montemarano, B.P. Sack, J.P. Gudas, M.G. Vassilaros, H.H. Vanderveldt, High strength low alloy steels in naval construction, J. Sh. Prod. Des. 2 (1986) 145–162.

[53] W. Bendick, J. Gabrel, B. Hahn, B. Vandenberghe, New low alloy heat resistant ferritic steels T/P23 and T/P24 for power plant application, Int. J. Press. Vessels Pip. 84 (2007) 13–20.

[54] T. Pardoen, J.W. Hutchinson, An extended model for void growth and coalescence, J. Mech. Phys. Solids 48 (2000) 2467–2512.

[55] Y. Tang, E.M. Bringa, M.A. Meyers, Ductile tensile failure in metals through initiation and growth of nanosized voids, Acta Mater. 60 (2012) 4856–4865.

[56] E. Alexopoulos, Introduction to multivariable regression analysis, Hippokratia 14 (2010) 23–28.

[57] W. Liu, Z. Wang, X. Liu, N. Zeng, Y. Liu, F.E. Alsaadi, A survey of deep neural network architectures and their applications, Neurocomputing 235 (2017) 11–26.

[58] A. Krizhevsky, I. Sutskever, G.E. Hinton, ImageNet classification with deep convolutional neural networks, in: International Conference on Neural Information Processing Systems, Lake Tahoe, NV, USA, 2012, pp. 1097–1105.

[59] D.W. Ha, C.Y. Jeong, Effect of pre-straining on the high-cycle fatigue properties of hot-rolled steel sheets for automotive structural uses, Korean J. Met. Mater. 56 (2018) 177–186.